This article has been accepted for publication in a future issue of this journal, but has not been fully edited. Content may change prior to final publication. Citation information: DOI 10.1109/TPEL.2021.3107546, IEEE Transactions on Power Electronics

Winding Layout Considerations for an Integrated Generator-Rectifier System

Phuc Huynh, *Student Member, IEEE*, Anjana J. Samarakoon,
Kiruba S. Haran, *Fellow, IEEE* and Arijit Banerjee, *Senior Member, IEEE*

An integrated generator-rectifier system is a promising architecture to harvest energy in offshore wind turbines. The system processes the majority of the incoming power using reliable, efficient, and inexpensive passive diodes operating at generator line frequency. Elimination of capacitors at the diode rectifiers' output by appropriately phase shifting the voltages of a multi-port generator further improves the reliability of the overall architecture. This paper creates a generalized framework to evaluate the interactions among the different generator ports, diode-bridge rectifiers, and the active rectifier that is used to control the power flow. The framework enables quantifying the effect of integration on the dc-bus power ripple and power imbalance among different generator ports. An exemplary winding layout is proposed that ensures theoretically zero interaction between the passive ports though all the ports are mounted on a magnetic structure. A 10 MW integrated generator-rectifier design and simulation proves the accuracy of the framework using coupled circuit-and-finite-element simulation. Finally, a laboratory prototype shows the realization of the winding layout. The proposed inductance-matrix based framework can be used to evaluate other winding layouts to estimate the effect of magnetic coupling on the system's performance.

***Index Terms*—Ac-dc power conversion, dc power systems, generators, permanent magnet machines, power conversion, rectifiers, wind energy, wind energy generation**

I. Introduction

Offshore wind is an emerging renewable energy resource with rapidly increasing installed capacity [1]–[4]. Direct-drive, permanent-magnet synchronous generators (PMSGs) with full power converters have been the preferred choice for energy harvesting [5]–[10]. For example, Gamesa 10X, GE Haliade X, Vestas V164, rated between ten and fourteen MWs, adopt this architecture [11]–[13].

In contrast, an integrated generator-rectifier architecture reduces the amount of power processed by the active rectifier by extensively using passive diodes operating at the generator line frequency [14], [15]. The series-stack architecture is shown in Fig. 1. The passive rectifiers process 60% of the total power while the active rectifier regulates the power flow to achieve the turbine maximum power point tracking (MPPT). The reduction in active rectification along with the elimination of passive-rectifier bulky filter capacitors by phase-shifting the generator back electro-motive-forces (emfs) improve the overall system power density, efficiency, and reliability.

The information, data, or work presented herein was supported by the Advanced Research Projects Agency-Energy (ARPA-E), U.S. Department of Energy, under Award DE-AR0001057. The authors would also like to thank the Grainger Center for Electric Machinery and Electromechanics for partially funding this project.

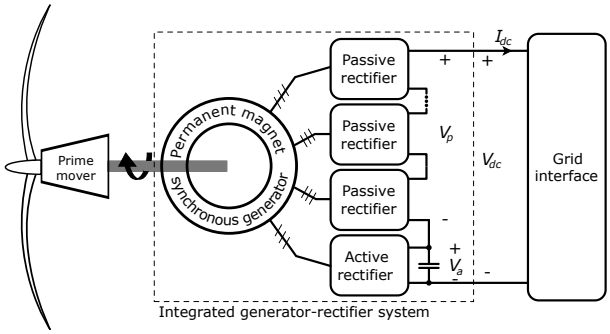

Fig. 1. Integrated generator-rectifier system based on a multi-port PMSG. The generator powers one active rectifier in series with multiple passive rectifiers. The turbine (prime mover) mechanical power is converted to dc electrical power and then delivered to a dc grid interface.

The design, analysis, and control of the integrated generator-rectifier system previously considered the multi-port generator as isolated ac ports modeled using a series resistance, inductance, and a speed-dependent voltage source (RLE). However, the generator-rectifier interaction is complex, especially when the ac ports are magnetically coupled. The key contribution of this paper is an analytical framework to capture the interaction between different generator ac ports and the rectifiers by considering the complete generator inductance matrix, capturing all self and mutual inductances. Requirements on the inductance matrix are derived to ensure the isolated-RLE model's validity from a design and control perspective, even in the presence of magnetic coupling among different ac ports. The analysis reveals a trade-off between the dc bus power ripple and the power imbalance between the active and passive sections of the generator. Finally, a fractional-pole-pitch winding layout is proposed as an example to provide a required 20^o phase shift among the passive ports, while achieving a complete magnetic decoupling from an equivalent circuit standpoint. The desired properties are verified using a generator finite-element-analysis (FEA) model at a 10-MW power level. A simulation coupling the FEA model to the rectifier circuit proves that a low dc-bus power ripple and a low generator torque are simultaneously achieved. The fractional-pole-pitch structure is also experimentally implemented at a low power level. The analysis paves the way for development of other machine topologies that are guaranteed to work with the integrated rectifier system.

The rest of this paper is organized as follows: Section II provides the theoretical analysis of the generator to ensure the decoupling between different phases from the circuit perspec-

This article has been accepted for publication in a future issue of this journal, but has not been fully edited. Content may change prior to final publication. Citation information: DOI 10.1109/TPEL.2021.3107546, IEEE Transactions on Power Electronics

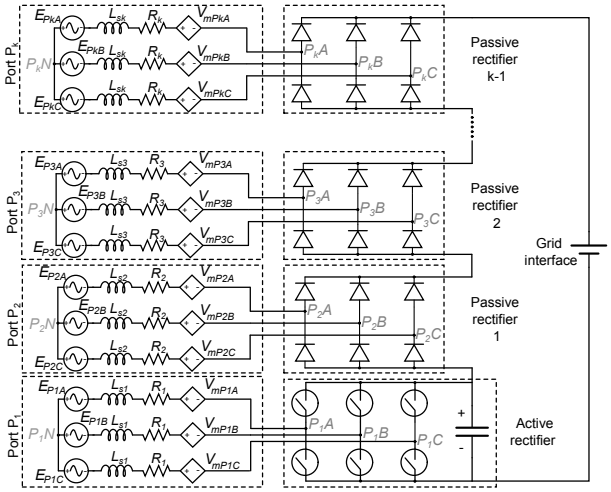

Fig. 2. Electrical circuit representation of an integrated generator rectifier system.

tive. Based on the per-unit system developed in Section II, Section III highlights the benefits of the integrated generator-rectifier systems compared to other alternatives for high-power ac-to-dc conversion. Section IV discusses an exemplary generator winding layout that meets the theoretical requirement. Section V verifies the proposed configuration via a coupled circuit–and–finite-element simulation. Finally, a low-power experimental setup is exhibited in Section VI.

II. Framework for Generator and Rectifier Integration

This section presents a generalized circuit representation of the integrated generator-rectifier system considering the magnetic coupling across all the generator phases. Conditions for the magnetic decoupling are derived assuming that the neutral points of all the ac ports are electrically isolated. Under these constraints, the active rectifier could be controlled as a dc current source and the passive-rectifier ac ports are representable using RLE equivalent circuits. A per-unit circuit is then constructed to evaluate the dc-bus power ripple and the output-power imbalance between one passive and the active ports. Finally, a trade-off is established between these two quantities. This trade-off curve can be used as an additional input to the generator design to achieve a specific dc-bus power ripple and output power ratio between the active and passive ports.

A. Generalized Circuit Representation of The Integrated Generator-rectifier System

Fig. 2 shows the generalized circuit representation of an integrated generator-rectifier system based on a k-port generator with the magnetic coupling represented using current-dependent voltage sources. Port P_1 powers an active rectifier, and the others are each connected to a three-phase passive rectifier without an output capacitor. Each phase in an ac port is modeled by a speed-dependent back emf source, a self inductance, a resistance, and the current-dependent voltage source, all connected in series. In general, the phase-A back emf of port P_i is

$$E_{PiA} = E_i \sin(\omega t + \theta_i) \tag{1}$$

where E_i is the amplitude, ω is the electrical frequency, and θ_i the relative phase shift between port P_i and port P_2. The phase-B and phase-C back emfs of each port lag the phase-A back emf by $2\pi/3$ and $4\pi/3$, respectively. An appropriate θ_i among different passive ports reduces the total passive-port voltage ripple, thereby, eliminating the need for bulky dc-side filter capacitors to smooth the output power [16]. It will be shown in Section IV that the necessary phase shift is achieved using a specific winding layout.

The current-dependent voltage source in each phase captures the induced voltage on the phase due to current variation in all the other phases, including the one from different ac ports. For example, the induced voltage on port P_i phase-A is:

$$V_{mPiA} = \underbrace{L_{PiA,PiB}\frac{dI_{PiB}}{dt} + L_{PiA,PiC}\frac{dI_{PiC}}{dt}}_{V'} + \underbrace{\sum_{j=1\ldots k\ j\neq i,\ X\in\{A,B,C\}} L_{PiA,PjX}\frac{dI_{PjX}}{dt}}_{V''} \tag{2}$$

where j indexes all other ports, $L_{PiA,PjX}$ represents the mutual inductance between phase A of the P_i port and phase X of the P_j port (X could be either A, B, or C), and I_{PjA} denotes the phase-A current in port P_j.

B. Conditions to Decouple Different Generator ac Ports

From a circuit standpoint, the phases are decoupled if the current-dependent voltage source in one phase is representable only as a function of the current in the same phase.Evident from (2), the voltage comprises two components, one due to different phases within the same ac port, and the other from the different ac ports. The currents in each port are always balanced due to the neutral point isolation, e.g., $I_{PiA} + I_{PiB} + I_{PiC} = 0,\ \forall i = 1..k$. Dependency of V' on other phase currents is eliminated by keeping the mutual inductances between any two phases within the same ac port equal, e.g., $L_{PiA,PiB} = L_{PiA,PiC}$. V'' is eliminated by ensuring identical mutual inductances between any two ac ports, e.g., $L_{PiA,PjA} = L_{PiA,PjB} = L_{PiA,PjC}$. With these conditions, (2) reduces to

$$V_{mPiA} = -M_i\frac{dI_{PiA}}{dt} \tag{3}$$

where M_i is the mutual inductance between any two phases of port P_i. Therefore, the per-phase voltage between nodes P_iN and P_iA in Fig. 2 becomes

$$V_{P_iN,P_iA} = E_{PiA} + L_i\frac{dI_{PiA}}{dt} + R_iI_{PiA} \tag{4}$$

where $L_i = L_{si} - M_i$ represents the equivalent inductance with L_{si} being the self inductance of the P_i port. This voltage equation represents an RLE model for phase-A of port P_i.

The magnetic decoupling could be achieved for all the other phases if the inductance matrix follows the form in

This article has been accepted for publication in a future issue of this journal, but has not been fully edited. Content may change prior to final publication. Citation information: DOI 10.1109/TPEL.2021.3107546, IEEE Transactions on Power Electronics

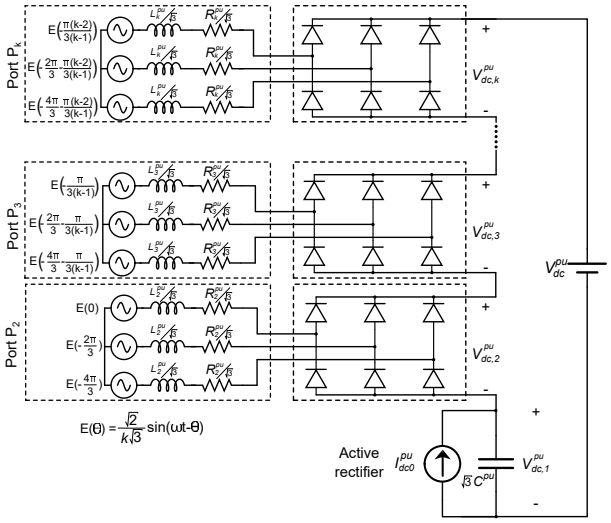

Fig. 3. Equivalent circuit of the integrated generator-rectifier system considering the control strategy. Parameters are expressed in per-unit.

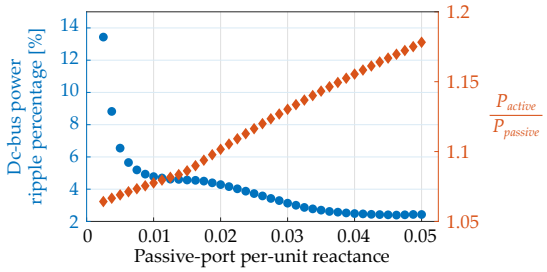

Fig. 4. Consider a 4-port generator with $R_i^{pu} = 0.011$, and $C^{pu} = 0.01$. Dc-bus power ripple decreases as the per-port per-unit reactance increases. Simultaneously, the active rectifier delivers more power compared to the passive rectifier, expressed by the increasing trend of the orange diamonds.

Table I. Under this condition, the integrated generator-rectifier system is representable by the simplified circuit in Fig. 3. The active rectifier can draw constant power because the equivalent inductances and resistances of all the phases are identical. Therefore, it is represented by an ideal current source in parallel with a capacitor [16]. In addition, all the mutual voltages are eliminated. Parameters for the circuit are derived next.

C. Per-unit Equivalent Circuit

A per-unit equivalent representation eliminates the need for actual voltage and actual power for circuit analysis. This circuit is useful because the generator per-unit reactance is terminal-voltage and output-power independent [17]. The generator stack length and number of turns could be scaled to meet the power and voltage levels without affecting the rectifier system features, such as the power percentage processed by the active rectifier, the power imbalance between the ac ports, and the dc-bus power ripple percentage.

The first step to develop the circuit is to define the base quantities. The base voltage is defined as

$$V_{base} = \sum_{i=1..k} \frac{E_i\sqrt{3}}{\sqrt{2}} \quad , \quad \text{and} \quad P_{base} = P_{rated} \tag{5}$$

where E_i is the line-to-neutral peak back emf of port P_k and P_{rated} is the rated output power. The derived base current and impedance are

$$I_{base} = \frac{P_{base}}{\sqrt{3}V_{base}} \quad , \quad \text{and} \quad Z_{base} = \frac{V_{base}}{\sqrt{3}I_{base}}. \tag{6}$$

The second step is to normalize the actual equations by the base values. For example, normalizing both sides of (4) by the defined V_{base}, normalizing current terms by the defined I_{base} and factoring out the base impedance, the per-unit representation is

$$V_{PkN,PkA}^{pu} = E_{PkA}^{pu} + \frac{L_k^{pu}}{\sqrt{3}}\frac{dI_{PkA}^{pu}}{dt} + \frac{R_k^{pu}}{\sqrt{3}}I_{PkA}^{pu} \tag{7}$$

The same normalization is applied for all other RLE branches from Fig. 3. The development is completed with the capacitor equation:

$$I_C = C\frac{dV_C}{dt} \tag{8}$$

where C is the capacitance of the high-frequency filter capacitor. Normalizing both sides of (8) by I_{base} and V_C by V_{base}, as well as collecting the terms using Z_{base}:

$$I_C^{pu} = \frac{\sqrt{3}C}{Z_{base}}\frac{dV_C^{pu}}{dt} = \sqrt{3}C^{pu}\frac{dV_C^{pu}}{dt}. \tag{9}$$

The per-unit equation is identical to the original equation, except that the factor $1/\sqrt{3}$ appears with each per-unit inductance and resistance term, and the factor $\sqrt{3}$ appears with the per-unit capacitance term, as shown in Fig. 3. The back emfs of all phases are assumed to be identical. Therefore, each has the normalized amplitude of $\frac{\sqrt{2}}{k\sqrt{3}}$ with the appropriate phase angle.

D. Trade-off between the ac Ports Power Imbalance and the dc-bus Power Ripple

The circuit shown in Fig. 3 captures both power ripple on the dc-bus and the amount of power delivered by each ac port. Quantification of these values requires the active-rectifier dc-output current I_{dc0}^{pu} and the per-unit dc-bus voltage V_{dc}^{pu}. Due to the base power being delivered at the dc bus, $V_{dc}^{pu}V_{base}I_{dc0}^{pu}I_{base} = P_{base}$. By definition (6), the product between the per-unit dc-bus voltage and the per-unit active-rectifier dc-side current is constant:

$$V_{dc}^{pu}I_{dc0}^{pu} = \sqrt{3}. \tag{10}$$

The dc-bus voltage is calculated to ensure the active rectifier has sufficient dc voltage to operate. In the serially-connected system, each passive rectifier generates a dc voltage

$$\underbrace{V_{dc,i}^{pu}}_{i\,=\,2..k} = \underbrace{\frac{3}{\pi}\frac{\sqrt{2}}{k}}_{\text{back emf contribution}} - \underbrace{\frac{3}{\pi}\frac{\omega L_i^{pu}}{\sqrt{3}}I_{dc0}^{pu}}_{\text{commutation drop}} - \underbrace{2\frac{R_i^{pu}}{\sqrt{3}}I_{dc0}^{pu}}_{\text{resistive drop}}. \tag{11}$$

This article has been accepted for publication in a future issue of this journal, but has not been fully edited. Content may change prior to final publication. Citation information: DOI 10.1109/TPEL.2021.3107546, IEEE Transactions on Power Electronics

Table I
REQUIRED INDUCTANCE MATRIX FOR RLE REPRESENTATION OF ALL GENERATOR PHASES

Phase	A_{P1}	B_{P1}	C_{P1}	A_{P2}	B_{P2}	C_{P2}	...	A_{Pk}	B_{Pk}	C_{Pk}
A_{P1}	L_{s1}	M_1	M_1	M_{12}	M_{12}	M_{12}	...	M_{1k}	M_{1k}	M_{1k}
B_{P1}	M_1	L_{s1}	M_1	M_{12}	M_{12}	M_{12}	...	M_{1k}	M_{1k}	M_{1k}
C_{P1}	M_1	M_1	L_{s1}	M_{12}	M_{12}	M_{12}	...	M_{1k}	M_{1k}	M_{1k}
A_{P2}	M_{12}	M_{12}	M_{12}	L_{s2}	M_2	M_2	...	M_{2k}	M_{2k}	M_{2k}
B_{P2}	M_{12}	M_{12}	M_{12}	M_2	L_{s2}	M_2	...	M_{2k}	M_{2k}	M_{2k}
C_{P2}	M_{12}	M_{12}	M_{12}	M_2	M_2	L_{s2}	...	M_{2k}	M_{2k}	M_{2k}
...	...	...	...	...	...	...	...	...	...	...
A_{Pk}	M_{1k}	M_{1k}	M_{1k}	M_{2k}	M_{2k}	M_{2k}	...	L_{sk}	M_k	M_k
B_{Pk}	M_{1k}	M_{1k}	M_{1k}	M_{2k}	M_{2k}	M_{2k}	...	M_k	L_{sk}	M_k
C_{Pk}	M_{1k}	M_{1k}	M_{1k}	M_{2k}	M_{2k}	M_{2k}	...	M_k	M_k	L_{sk}

	Active port	Passive port
Active port	$\mathbf{L_{AA}}$	$\mathbf{L_{AP}}$
Passive port	$\mathbf{L_{AP}^T}$	$\mathbf{L_{PP}}$

where ω is the rated electrical frequency [18]. The active-rectifier dc-side voltage must be the peak line-to-line back emf to maintain controllability under the space-vector-modulation scheme while minimizing the voltage rating, or

$$V_{dc,1}^{pu} = \frac{\sqrt{2}}{k}. \tag{12}$$

By KVL, the dc-bus voltage is

$$V_{dc}^{pu} = \sum_{i=1..k} V_{dc,i}^{pu}. \tag{13}$$

Substituting (11) and (12) into (13) as well as using (10), the per-unit dc-bus voltage follows:

$$V_{dc}^{pu} = \frac{\sqrt{2}}{k} + \frac{3}{\pi}\frac{\sqrt{2}}{k}(k-1) - \sum_{i=2..k}\left(\frac{3}{\pi}\frac{X_{Li}^{pu}}{V_{dc}^{pu}} + 2\frac{R_i^{pu}}{V_{dc}^{pu}}\right) \tag{14}$$

where $X_{Li}^{pu} = \omega L_i^{pu}$ represents the per-unit equivalent reactance of each phase in port i. The per-unit dc-bus voltage is calculated by solving the quadratic equation (14). The dc-bus average current is calculated using (10) to complete the parameters in Fig. 3.

Fig. 4 shows the dc-bus power ripple and the output power ratio between one passive port and the active port as a function of X_{Li}^{pu} using the per-unit circuit in Fig. 3. The results are generated assuming a four-identical-ac-port machine, i.e., $k = 4$, with $R_i^{pu} = 0.011$. The filter capacitor is $C^{pu} = 0.01$. As the per-unit reactance increases, the dc-bus power ripple decreases because the rate of current commutation in the ac port is reduced. In addition, less power is delivered through the passive rectifier because the output dc-bus voltage is reduced as the inductance increases, as shown in (11). Therefore, the ratio between the output power of the active port and that of the passive port increases.

III. COMPARISON BETWEEN THE INTEGRATED GENERATOR-RECTIFIER SYSTEM AND THE ALTERNATIVES

This section highlights the benefits of the integrated generator-rectifier system considering a limited-speed-range operation in a wind-turbine application. Next, a comparison against the conventional alternatives is presented to quantify these advantages. The generator's back emf amplitude is linearly dependent on the generator speed. As a result, the dc-side voltage of each passive rectifier is

$$\underbrace{V_{dc,i}^{pu}(\omega^{pu})}_{i\,=\,2..k} = \underbrace{\frac{3}{\pi}\frac{\sqrt{2}}{k}\omega^{pu}}_{\text{back emf contribution}} - \underbrace{\frac{3}{\pi}\frac{\omega\omega^{pu}L_i^{pu}}{\sqrt{3}}(\omega^{pu})^3 I_{dc0}^{pu}}_{\text{commutation drop}} - \underbrace{2\frac{R_i^{pu}}{\sqrt{3}}(\omega^{pu})^3 I_{dc0}^{pu}}_{\text{resistive drop}} \tag{15}$$

where ω^{pu} is the per-unit generator speed. The term $\omega\omega^{pu}L_i^{pu}$ relates the inductance to the speed. In addition, $(\omega^{pu})^3 I_{dc0}^{pu}$ represents output power of a wind turbine at maximum power, which is proportional to the cube of the rotational speed in a wind-turbine application [8]. Even though the generator operates at variable speed, the dc-bus voltage as calculated by (14) is maintained constant across the entire operating speed range by a grid-side converter [16]. The difference between the dc-bus voltage and the total passive-rectifier output is the active-rectifier dc-side voltage, which is speed dependent:

$$V_{dc,1}^{pu}(\omega^{pu}) = V_{dc}^{pu} - \sum_{i=2..k} V_{dc,i}^{pu}(\omega^{pu}). \tag{16}$$

Fig. 5(a) shows the dc-side voltage of the active rectifier by the blue-dash line for a four-port integrated generator-rectifier system with $X_{L,i}^{pu} = 0.025$ and the phase resistance neglected. The maximum dc-side voltage happens at the minimum generator speed, which sets the active-rectifier's rated voltage to be 0.75 pu. In a conventional one-port system, the active-rectifier rated voltage is $\sqrt{2}$ pu using (14).

The maximum current in an active-rectifier happens on the ac-side. The peak ac-side current is determined by the power balance relationship between the ac and dc sides:

$$\frac{3}{2}E_1^{pu}(\omega^{pu})I_{d,1}^{pu}(\omega^{pu}) = V_{dc,1}^{pu}(\omega^{pu}) \times (\omega^{pu})^3 I_{dc0}^{pu} \tag{17}$$

where E_1^{pu} is the per-unit peak line-neutral back emf of the ac port powering the active rectifier. $I_{d,1}^{pu}$ is the d-axis current of the active-rectifier ac-side currents with the d-axis aligned with the phase-A back emf. This d-axis current is the same as the peak ac-side current when the unity power-factor current-control strategy is implemented. The d-axis current is regulated by a controller such that the dc-bus current delivers a power that is proportional to the cube of the generator rotational speed [16]. Fig. 5(a) shows the peak ac-side current of the

This article has been accepted for publication in a future issue of this journal, but has not been fully edited. Content may change prior to final publication. Citation information: DOI 10.1109/TPEL.2021.3107546, IEEE Transactions on Power Electronics

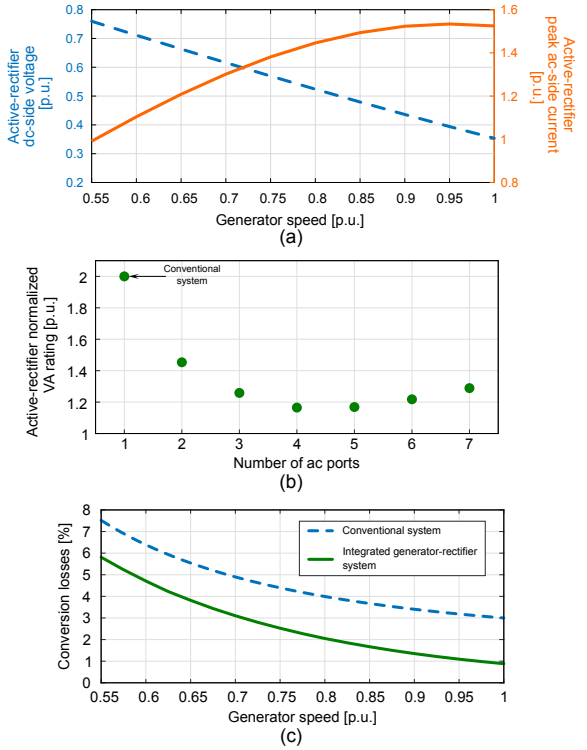

Fig. 5. Key characteristics of the integrated generator-rectifier system: (a) voltage and current of the partial-power-rated active rectifier based on a four-port generator with 0.025 pu per-phase reactance. (b) Variation in voltage and current ratings reduced the active-rectifier VA rating compared to the conventional all-active-rectifier topologies. (c) The conversion losses are reduced across the entire generator's operating speed range as the majority of the power is processed on the high-efficiency passive rectifiers.

active rectifier for the four-port integrated generator-rectifier system. In a conventional one-port system, the rated current is $\sqrt{2}$ pu.

The curves for the active-rectifier's voltage and current requirements could be constructed using (16) and (17) for each number of ac ports and a given per-unit reactance. Subsequently, the volt-ampere (VA) rating is calculated *as the product between the maximum required voltage and current*. The VA rating indicates the active-rectifier size. Fig. 5(b) shows the VA ratings as a function of the number of ac ports for a system with a total per-unit reactance of 0.1 pu, which equally splits among different ports. An integrated system based on a four-port generator results in the minimum VA rating — 1.19 pu compared to 2 pu of a conventional system, equivalent to a 40% reduction. As the majority of the power is processed on highly-efficient diodes, the overall conversion losses are significantly reduced, as shown in Fig. 5(c) [19]. At the rated condition, the losses are reduced by 60%, from 3% to 1%.

Table II compares the integrated generator-rectifier system and other alternatives for high-power ac-to-dc conversion. From the power electronics perspective, diode bridge is the most simple, reliable, and efficient but without control capability. The two-level pulse-width modulation (PWM) and three-level neutral-point-clamped (NPC) converters are the most common alternatives. The first choice requires the switch to

Table II
COMPARISONS OF DIFFERENT ARCHITECTURES FOR HIGH POWER AC-TO-DC CONVERSION [14]

	Integrated generator -rectifier	Six-pulse diode rectifier	Two-level converter	Neutral -point clamped converter
Number of active switches	6	0	6	12
Active switch voltage rating	$< 0.4V_{dc}$	—	V_{dc}	0.5 V_{dc}
Power processed on active switches	$< 30\%P_{dc}$	0	P_{dc}	P_{dc}
Conversion loss	$< 1\%$	0.3%	3.2%	3% [20]
Dc-bus control	Yes	No	Yes	Yes

be rated for the entire dc-bus voltage and the peak ac-side current. Parallel- and series-connecting multiple devices are typically required to reach MW-power level due to device's limited available voltage and current ratings. Consequently, the reliability is compromised because complex circuit board layout and additional circuitry are required to ensure even voltage/ current sharing [6]. NPC converters reduces the individual switch voltage or current rating but potentially leads to pre-mature failure at the hot spots due to uneven loss distribution [21]. From a machine standpoint, multi-port generators have been used to connect several active rectifiers in parallel, thereby reducing each individual active-rectifier size [22]. However, in this architecture, the entire power must be processed by active-switching devices. In comparison, the proposed integrated generator-rectifier system processes the majority of the power using diodes, leading to its high power density, efficiency, and reliability.

IV. AN EXEMPLARY GENERATOR WINDING LAYOUT SATISFYING THE INDUCTANCE MATRIX REQUIREMENT

This section proposes a winding layout that meets the inductance matrix requirement in Table I for a four-port generator. Fig. 6 shows a conceptual design, comprising two structures that are axially split. The left section creates one ac port powering the active rectifier. The right section creates three ac ports, 20^o phase-shifted from each other to minimize the dc-bus power ripple [23], [24], powering three passive rectifiers. The axial split eliminates the mutual inductance between the active-rectifier ac port and passive-rectifier ac ports. Mutual inductances among the passive-rectifier ac ports are eliminated by designing a winding layout based on fractional-pole-pitch coils.

A. Passive-rectifier Port Winding Configuration

Non-overlapping fractional-pole-pitch coils are selected to achieve multiple passive-rectifier ac ports with appropriate phase shift and zero mutual inductance. The top view of the coil structure is shown in Fig. 7 with X denoting the going

This article has been accepted for publication in a future issue of this journal, but has not been fully edited. Content may change prior to final publication. Citation information: DOI 10.1109/TPEL.2021.3107546, IEEE Transactions on Power Electronics

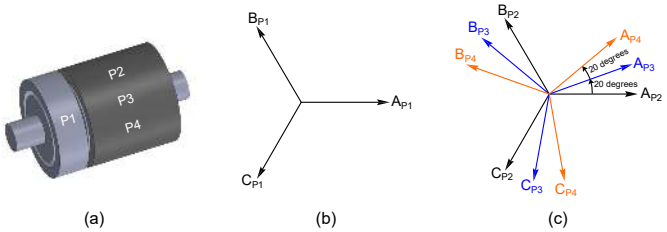

Fig. 6. (a) Conceptual cartoon of an axially-split generator suitable for integrated rectification, (b) voltage vectors of the active-rectifier port P_1, (c) voltage vectors of passive-rectifier ports P_2, P_3, and P_4.

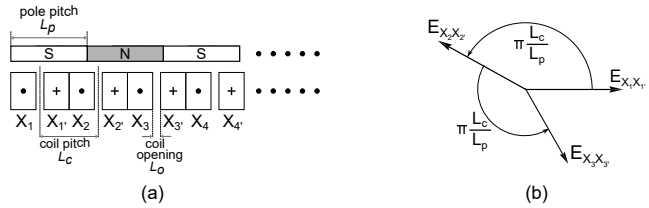

Fig. 7. (a) Winding configuration of the passive-rectifier ac port. (b) The corresponding back emfs vectors.

and X' denotes the returning coil side. Assuming the back emf on the coil X_1X_1' is

$$E_{X_1X_1'} = E_0 \cos(\omega t), \tag{18}$$

where E_0 is the amplitude and ω is the electrical frequency. The coil pitch, distance between two adjacent coil centers, is denoted by L_c and the pole pitch is denoted by L_p. The back emf of the k-th coil is:

$$E_{X_kX_k'} = E_0 \cos\left(\omega t - \pi(k-1)\frac{L_c}{L_p}\right) \tag{19}$$

where coil 1 is selected as the reference, e.g., having zero phase angle. Fig. 7(b) shows back emfs of coils 1, 2, and 3. Back emfs of other coils could also be expressed but are omitted for simplicity.

The relationship between the magnet pole pitch and coil pitch sets the machine periodicity [25]. The total magnet pitch and coil pitch must be the same to wrap the linear structure shown in Fig. 7 into a cylindrical structure. Therefore, the coil pitch and the magnet pitch are related by

$$nL_c = pL_p \tag{20}$$

where n is an integer and p is an even integer number, denoting number of coils and number of magnetic poles, respectively.

The phase windings are constructed by appropriately connecting the individual coils to achieve the voltage vectors shown in Fig. 6(c). For example, consider $\frac{L_c}{L_p} = \frac{26}{18}$. Using (19), the angular position of the k-th coil back emf is $(k-1)\pi\frac{26}{18}$ radians or $(k-1)260$ degrees. Using (20), the machine needs to have 18 coils and 26 poles, or an integer multiple of these numbers. All the back emfs cover 360° with any two adjacent vectors to be 20° apart, as shown in Fig. 8(a). The available back emf are connected to form three three-phase sets following Fig. 8(b). For example, phase A_{P2} is $E_1 - E_{10}$, formed by connecting coils X_1X_1' and $X_{10}X_{10}'$ in opposite polarity, as shown in 8(c). Similar connections are

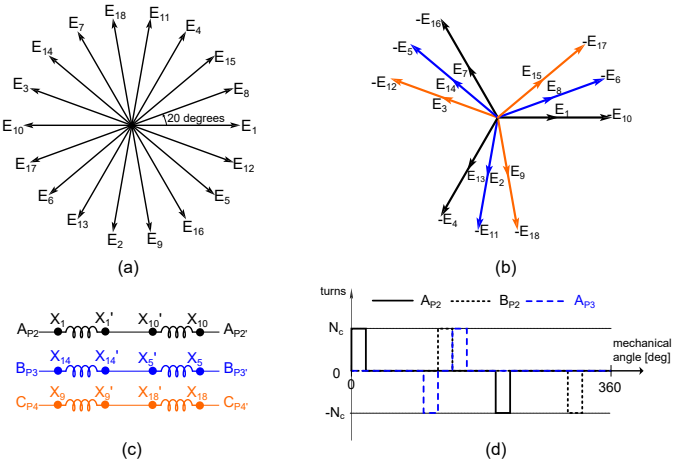

Fig. 8. A structure with $\frac{L_c}{L_p} = \frac{26}{18}$: (a) available voltage vectors, (b) formation of three three-phase winding sets with 20° phase shift, (c) physical connection pattern, (d) non-zero part of the winding functions for different phases do not overlap.

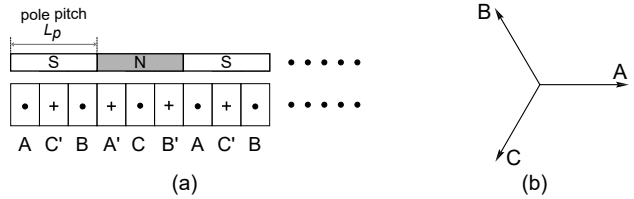

Fig. 9. (a) Active-rectifier ac port winding configuration. (b) The corresponding voltage vectors.

made to form other phases.

The foregoing method for coil connection leads to zero mutual inductance. Mutual inductance between two windings depends on the average of the product between the two corresponding winding functions [26], [27]. Winding functions for phases A_{P2}, B_{P2}, and A_{P3} with the given connection pattern are shown in Fig. 8(d). The winding function for each phase consists of two non-zero, bi-polar intervals. In the proposed configuration, the product of any two winding functions is zero, leading to the zero mutual inductance. The inductance matrix corresponding to the passive ports, matrix $\mathbf{L_{PP}}$, is diagonal, meeting the requirement in Table I with zero mutual M-terms.

B. Active-rectifier Winding Configuration

The active rectifier is axially split from the passive rectifier to eliminate the mutual coupling between the passive-rectifier phases and active-rectifier phases, i.e., all entries in the matrix $\mathbf{L_{AP}}$ are zero. A standard distributed winding is employed for the active-rectifier ac ports, as shown in Fig. 9(a). This winding approach results in a balanced three-phase back emf as shown in Fig. 9(b).

Section V corroborates the feasibility of the proposed winding layout by showing the implementation using an FEA model of a 10-MW generator, suitable for offshore wind turbines. The FEA model is then coupled to a circuit simulator to verify the impact of magnetic coupling among the different

This article has been accepted for publication in a future issue of this journal, but has not been fully edited. Content may change prior to final publication. Citation information: DOI 10.1109/TPEL.2021.3107546, IEEE Transactions on Power Electronics

phases on the dc-bus power ripple as well as the generator torque ripple.

V. FEA VERIFICATION OF THE PROPOSED WINDING LAYOUT FOR A 10 MW GENERATOR

The FEA verification focuses on the passive rectifier portion because of the non-conventional winding configuration. A generator design is first created using Altair Flux™ following the structure shown in Fig. 11(a). For the direct-drive generator, the inner rotor radius R is preferred to be as large as possible to increase the generator tip speed, thereby improving the power density. A six-meter radius is the practical constraint because an object of this size is the biggest that could fit in the existing vehicles. The airgap length is chosen to be 12 mm, following the design rule by the National Renewable Energy Laboratory (NREL) [4]. Two hundred sixty poles are chosen for convenience because one fundamental period of the machine requires 26 poles. This selection leads to the pole pitch of 145 mm, well within the range reported by NREL [4]. Each group or 26 poles corresponds to 18 stator coils to form the back emf vectors as shown in Fig. 8(a).

For each group of 18 consecutive coils, the connection pattern laid out in Fig. 8 is implemented to form nine phases. The same phase from each of the ten periods is serially connected to form a complete machine phase. The generator rated speed is chosen to be 9.6 rpm, typical for 10-MW direct-drive wind turbines. The current density is set as 4 A/mm^2 to facilitate air cooling. The magnets are Halbach type to reduce the rotor yoke size. The magnet thickness is selected to achieve 0.045 pu phase reactance. Using (14), the dc-bus voltage is 1.2 pu assuming $R_i^{pu} = 0.011$. As the dc-side voltage of the active rectifier is 0.35 pu, according to constraint (12), the active rectifier provides 2.9 MW of the total 10 MW power. The stack length is calculated for the passive-rectifier section to provide 7.1 MW. The dimensions are summarized in Fig. 11(b) and flux density of the structure is shown in Fig. 11(c).

Back emfs of port P_1, phase A of port P_2 and P_3 are shown in Fig. 10(d), confirming the desired 120° phase shift between phases in the same port and 20° phase shift between different ports. Fig. 10(e) shows the inductance matrix measured from the FEA model. The proposed connection pattern eliminates mutual coupling between different phases, as seen by the dominance of diagonal matrix elements.

A circuit simulation is created following Fig. 3 with the ac ports replaced by the Altair Flux^{TM} FEA model to evaluate the generator performance in the presence of the power electronics. Electrical parameters are calculated based on the back emf produced by the FEA model as shown in Fig. 10(c), the measured inductance as shown in Fig. 10(d), the base power of 10 MW, and the equations in Section II. Parameter values are summarized in Fig. 10(b).

The FEA verification shown in Fig. 11 confirms feasibility of the proposed generator configuration. The currents in port P_1 are shown in Fig. 11(a). The small ripple component during the conduction period of each phase is due to the phase-shifting effects. There is no substantial perturbation due to mutual coupling between different phases. The dc-bus current is shown in Fig. 11(b) with the ripple component at 18 times the back-emf fundamental frequency. The peak-to-peak ripple is 2.6% of the average current value, which agrees with the prediction using the per-unit circuit for the case $X_{Li}^{pu} = 0.047$, as shown in Fig. 4. The generator instantaneous torque is shown in Fig. 11(c). The peak-to-peak torque ripple is measured as 0.86% the average value. Next, Section VI shows an experimental verification to further corroborate the proposed winding layout.

VI. EXPERIMENTAL RESULTS

A. Experimental Setup

A low-power experimental setup was developed to verify the proposed generator topology, as shown in Fig. 12. The generator includes two assemblies, which are modified Samsung DC96-01218D PM motors mounted on custom-built frames. The original stator has 36 coils as shown in Fig. 12(b).

The assembly that powers the passive rectifier needs to provide a set of back emfs as shown in Fig. 6(c). The requirement is met with a custom-built 34-pole rotor. The magnets are enclosed by retaining rings, as shown in Fig. 12(c). The whole assembly is embedded inside the rotor frame, as shown in Fig. 12(d). Combined with the 36-coil stator, the modified machine has $L_c/L_p = p/n = 17/18$, according to (20) with $n = 36$ and $p = 34$. The phase difference between the back emfs of two consecutive coils is $\pi\frac{L_c}{L_p}$ or 170°, following (19). As the 170° phase difference between two consecutive coils repeats 36 times, the 360° interval is covered by vectors that are 10° apart, as illustrated in Fig. 12(e). The coil connection pattern to form the required three three-phase sets with a 20° phase-shift is shown in Fig. 12(f). Each phase is formed by serially connecting four coils, including out-of-phase pairs to eliminate mutual inductance. For example, phase A_{P1} is formed by serially connecting coils 1 and 18 in the same polarity and coils 19 and 36 in the opposite polarity. As a result, the total back emf is $E_{AP1} = E_1 + E_{18} - E_{19} - E_{36}$. Other phases are constructed in a similar manner.

Fig. 8(g) shows the complete experimental setup. The generator includes two assemblies, S1 and S2. S1 is the original machine with 48 magnetic poles powering the active rectifier Rec-1. S2 is the modified machine with 34 magnetic poles to form three phase-shifted ac ports. The three ports power three passive rectifiers, namely Rec-2, Rec-3, and Rec-4. Dc outputs of the active and the active rectifiers are serially connected to deliver power to an electronics load operating in a constant-voltage mode.

B. Generator Characteristics

The experimentally measured back emfs of the modified machine verify the space vectors in Fig. 12. The back emfs of individual coils 1, 2, 3, and 4 are shown in Fig. 13(a) when the generator rotates at 150 rpm. Back emfs of two consecutive coils (e.g, 1 and 2, or 2 and 3, etc) are phase-shifted by 170°, as predicted by (19). The connection pattern in Fig. 12(f) is implemented. Back emfs of phases A_{P2}, A_{P3}, and A_{P4} are recorded in Fig. 13(b), showing a 20° phase shift between different ac ports. In addition, the back emfs of phases A_{P2},

This article has been accepted for publication in a future issue of this journal, but has not been fully edited. Content may change prior to final publication. Citation information: DOI 10.1109/TPEL.2021.3107546, IEEE Transactions on Power Electronics

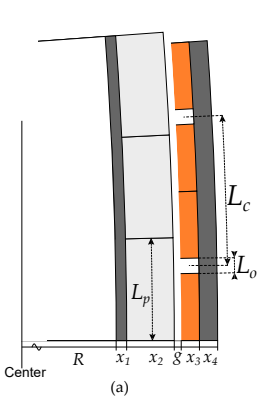

(a)

Quantity	Notation	Unit	Value
Magnet pole pitch	L_p	mm	147
Center-coil distance	L_c	mm	213.6
Coil-opening pitch	L_o	mm	22
Stack length	L_s	mm	1250
Rotor inner radius	R	mm	6000
Rotor yoke width	x_1	mm	15.6
Magnet width	x_2	mm	68
Air-gap width	g	mm	12
Coil width	x_3	mm	25.7
Stator yoke width	x_4	mm	25.7
Number of poles	N_p		260
Number of coils	N_c		280
Phase peak back emf	E_1	V	1934
Rated frequency	f_0	Hz	20.8
Base voltage	V_{base}	V	9475
Base power	P_{base}	MW	10
Base impedance	Z_{base}	Ω	9
Dc-bus voltage	V_{dc}	kV	11.5
Dc-bus current	I_{dc0}	A	869
Phase reactance	X_{Ll}^{pu}	pu	0.043
Phase resistance	R_s^{pu}	pu	0.011
Filter capacitance	C	mF	90

(b)

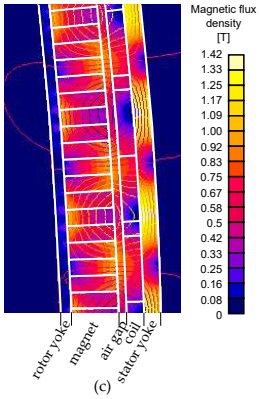

(c)

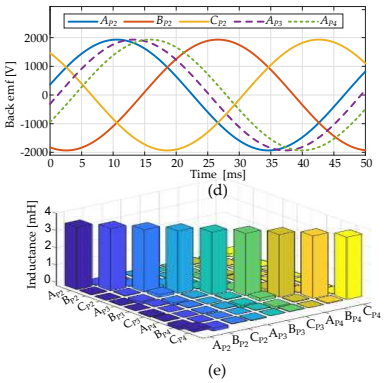

(d) (e)

Fig. 10. FEA verification of the proposed structure in Fig. 8: (a) Configuration of the generator FEA model. (b) Generator dimensions and the corresponding electrical quantities. (c) Flux density of the FEA model. (d) The induced back emf that has a 120° shift between phases in the same port and a 20° phase shift among different ports. (e) The inductance matrix is dominated by diagonal elements –self inductance– showing the magnetic decoupling between different phases.

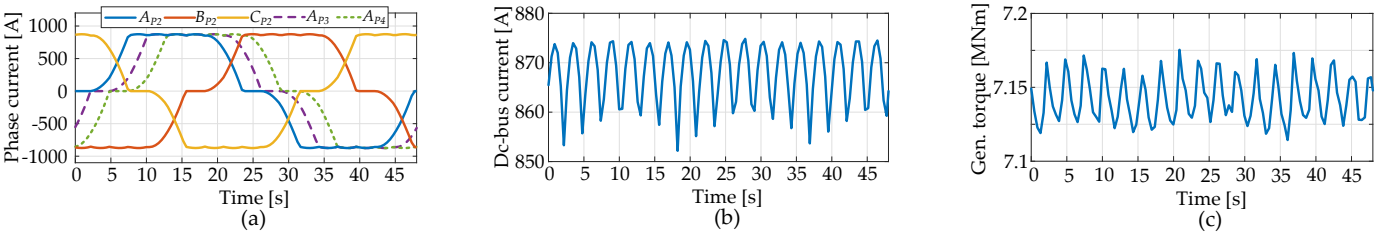

(a) (b) (c)

Fig. 11. Current and torque characteristics: (a) Currents in the passive rectifiers are trapezoidal and phase-shifted. (b) Dc-bus current has 2.4% peak-to-peak ripple at 18 times the fundamental back-emf frequency. (c) The peak-to-peak torque ripple is 0.86% of the average value.

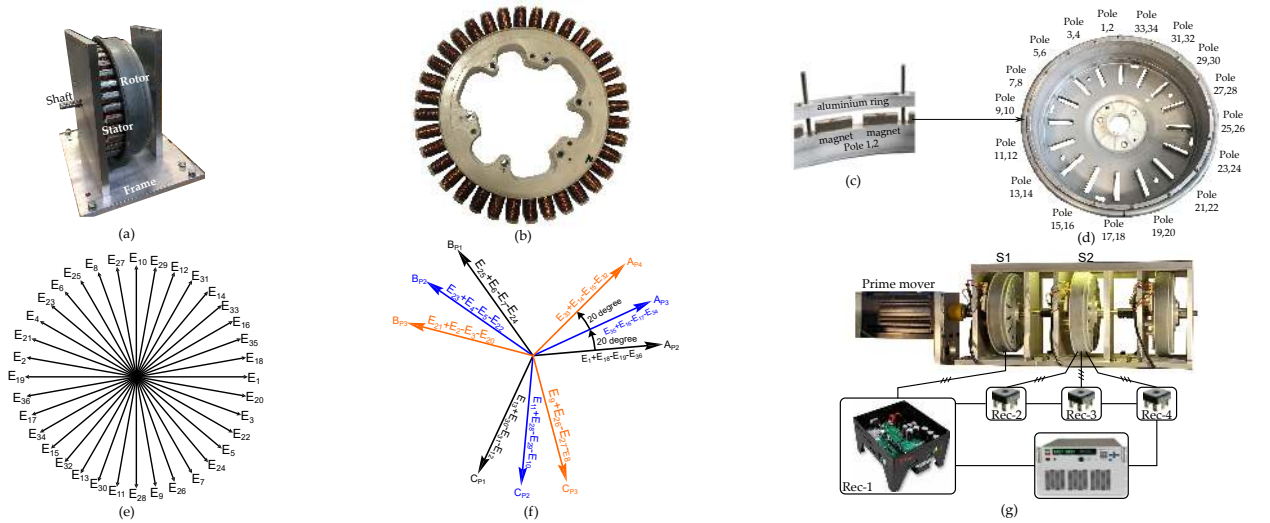

(a) (b) (c) (d) (e) (f) (g)

Fig. 12. Experimental setup: (a) machine assembly, (b) stator with 36 coils, (c) assembly view of the magnet ring, (d) complete magnet ring mounted on the original rotor frame, (e) back emf vectors of the 36-coil 34-pole combination, (f) connection pattern to achieve three three-phase sets shifted by 20° from each other, (g) complete experimental setup.

This article has been accepted for publication in a future issue of this journal, but has not been fully edited. Content may change prior to final publication. Citation information: DOI 10.1109/TPEL.2021.3107546, IEEE Transactions on Power Electronics

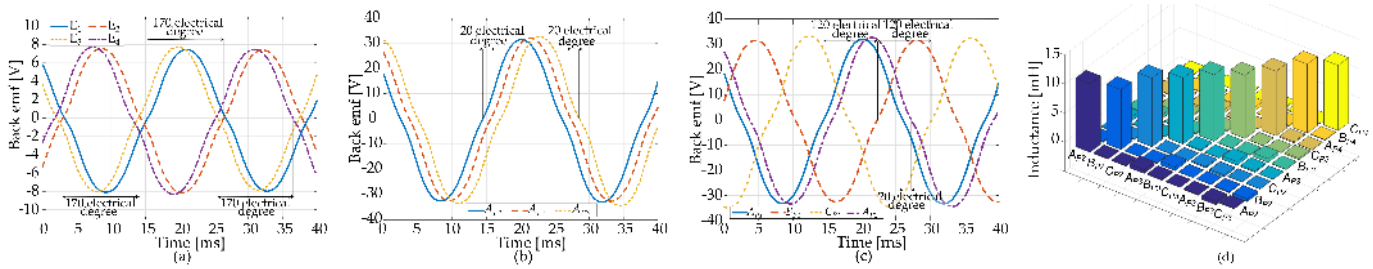

Fig. 13. Electrical characteristics of the experimental fractional-pole-pitch machine. (a) The consecutive coils shows 170° phase shift. Connection patterns in Fig. 12(f) result in (b) back emfs of phases A_{P2}, A_{P3}, and A_{P4} being phase-shifted by 20° from each other; and (c) back emfs of phases A_{P1}, B_{P1}, and C_{P1} being phase-shifted by 120° from each other. (d) Inductance matrix shows dominant diagonal components.

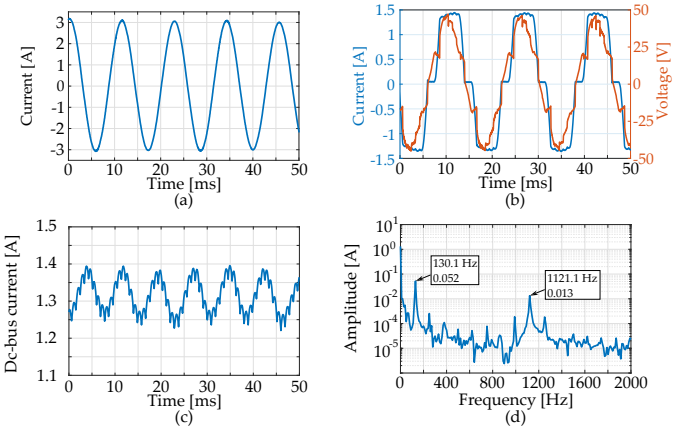

Fig. 14. Electrical characteristic of the integrated generator-rectifier system operating at 220 rpm and delivering 527 W to the dc bus. (a) Current is sinusoidal in the active port. (b) While the passive port back emf is sinusoidal, the phase current is trapezoidal due to operation of the capacitor-less diode bridge. (c) The dc bus experiences a low ripple current. (d) The dc-bus current frequency components.

B_{P2}, and C_{P2} in Fig. 13(c) show a 120° phase shift within the same ac port.

The inductance matrix of assembly S2 has dominant diagonal elements, as visualized in Fig. 13(d). The diagonal matrix verifies that the proposed generator configuration satisfies the RLE model (see Table I) and is appropriate to use in the integrated generator-rectifier system to reduce the dc-bus voltage ripple without requiring bulky filter capacitors.

C. Integrated Generator-rectifier Operation

Ac-dc conversion using the integrated generator-rectifier system is illustrated in Fig. 14. The outputs of the rectifiers are serially connected and deliver power to an electronics load operating in constant-voltage mode to maintain a 400-V dc-bus voltage. The prime mover turns the generator at 220 rpm. The active rectifier regulates sinusoidal current in the corresponding ac port and operates at unity power factor to minimize the volt-ampere rating. Fig. 14(a) shows the active rectifier phase-A current.

Dc-side current of the active-rectifier sets the current in the passive-rectifier ac ports [16]. Fig. 14(b) shows the current and voltage (relative to the neutral point) of port-2 phase-A. The current is trapezoidal because of the diode-bridge operation and closely mimics the simulation results in Fig. 14(a). The voltage and current are in phase due to elimination of the dc-side filter capacitor. The calculated power factor is 0.94, mostly due to the distortion factor.

Although the filter capacitors are eliminated, the dc-bus current has a low ripple component due to the phase shift between different passive rectifier ac ports, as shown in Fig. 14(c). There are two observable ripple components, one at 130 Hz and another one at 1121 Hz –18 times the line frequency, as shown in Fig. 13(d). The first is due to the generator imperfections, as shown by slight imbalance between back emfs in Fig. 13, while the second component is due to the back-emf phase shifting. A better construction of the machine would eliminate the first factor, resulting in a lower dc-bus power ripple. The total dc-bus current peak-to-peak ripple is 12.8% of the average value. A total power of 527 W is delivered to the electronic load.

VII. Conclusion

This paper proposes a generalized framework to quantify the effect of interaction between power electronic converters and a multi-port generator using an inductance matrix. Constraints on this matrix ensure the isolated RLE model's validity from a control and design perspective, even when the generator ports are magnetically coupled. A trade-off is shown between the dc bus power ripple and the power imbalance between the generator's active and passive ports. Intuitively, a higher generator inductance causes more voltage drop during the diode commutation leading to lower power being delivered by the passive ports. In contrast, a lower generator inductance increases the current commutation slope, resulting in a higher dc-bus power ripple. A 10 MW design using an exemplary winding layout shows the accuracy of the generalized framework. Further, a laboratory prototype using a fractional-slot winding proves the decoupling between different generator passive ports even when they locate on the same generator's magnetic structure. Table I can be used as a guideline to create new winding layouts suited for the integrated generator-rectifier systems.

References

[1] D. S. Ottensen, "Global offshore wind market report," Norweigian Energy Partner, Tech. Rep., 2018.

[2] C. Bak, R. Bitsche, A. Yde, T. Kim, M. H. Hansen, F. Zahle, M. Gaunaa, J. P. A. A. Blasques, M. Døssing, J.-J. W. Heinen *et al.*, "Light rotor: The 10-MW reference wind turbine," in *EWEA 2012-European Wind Energy Conference & Exhibition*. European Wind Energy Association (EWEA), 2012.

[3] P. Higgins and A. Foley, "The evolution of offshore wind power in the United Kingdom," *Renewable and sustainable energy reviews*, vol. 37, pp. 599–612, 2014.

[4] W. Musial, P. Beiter, P. Spitsen, J. Nunemaker, and V. Gevorgian, "2018 offshore wind technologies market report," National Renewable Energy Laboratory, https://www.energy.gov/eere/wind/downloads/2018-offshore-wind-market-report, Tech. Rep., 2018.

[5] A. Yazdani and R. Iravani, "A neutral-point clamped converter system for direct-drive variable-speed wind power unit," *IEEE Transactions on Energy Conversion*, vol. 21, no. 2, pp. 596–607, June 2006.

[6] F. Blaabjerg, M. Liserre, and K. Ma, "Power electronics converters for wind turbine systems," *IEEE Transactions on Industry Applications*, vol. 48, no. 2, pp. 708–719, March 2012.

[7] S. Li, T. A. Haskew, R. P. Swatloski, and W. Gathings, "Optimal and direct-current vector control of direct-driven PMSG wind turbines," *IEEE Transactions on Power Electronics*, vol. 27, no. 5, pp. 2325–2337, May 2012.

[8] M. Chinchilla, S. Arnaltes, and J. C. Burgos, "Control of permanent-magnet generators applied to variable-speed wind-energy systems connected to the grid," *IEEE Trans. Energy Convers.*, vol. 21, no. 1, pp. 130–135, March 2006.

[9] F. Rong, G. Wu, X. Li, S. Huang, and B. Zhou, "ALL-DC offshore wind farm with series-connected wind turbines to overcome unequal wind speeds," *IEEE Transactions on Power Electronics*, vol. 34, no. 2, pp. 1370–1381, 2019.

[10] S. Ye, D. Zhou, X. Yao, and F. Blaabjerg, "Component-level reliability assessment of a direct-drive PMSG wind power converter considering two terms of thermal cycles and the parameter sensitivity analysis," *IEEE Transactions on Power Electronics*, doi: 10.1109/TPEL.2021.3064363, 2021.

[11] Siemens Gamesa, "SG 10.0-193DD offshore wind turbine," Available: https://www.siemensgamesa.com/en-int/products-and-services/offshore/wind-turbine-sg-10-0-193-dd [Accessed: 15- Dec- 2019].

[12] GE Renewable Energy, "Haliade-X 12 MW offshore wind turbine platform," Available: https://www.ge.com/renewableenergy/wind-energy/offshore-wind/haliade-x-offshore-turbine [Accessed: 15- Dec- 2019].

[13] MHI Vestas Offshore Wind, "The world's most powerful available wind turbine gets major power boost," Available: http://www.mhivestasoffshore.com/worlds-most-powerful-available-wind-turbine-gets-major-power-boost/ [Accessed: 15- Dec- 2019].

[14] P. T. Huynh, P. J. Wang, and A. Banerjee, "An integrated permanent-magnet-synchronous generator–rectifier architecture for limited-speed-range applications," *IEEE Transactions on Power Electronics*, vol. 35, no. 5, pp. 4767–4779, 2020.

[15] P. Huynh and A. Banerjee, "Active voltage-ripple compensation in an integrated generator-rectifier system," *IEEE Transactions on Power Electronics*, vol. 36, no. 2, pp. 2270–2282, 2021.

[16] P. Huynh, S. Tungare, and A. Banerjee, "Maximum power point tracking for wind turbine using integrated generator-rectifier systems," *IEEE Transactions on Power Electronics*, vol. 36, no. 1, pp. 504–512, 2021.

[17] P. Huynh, S. Sirimanna, J. Mok, D. Lee, O. Ajala, S. Linares, D. Mulas, K. Haran, A. Dominguez-Garcia, G. Gross, and A. Banerjee, "Integrated generator-rectifier co-design for offshore wind turbines," in *2020 IEEE Energy Conversion Congress and Exposition (ECCE)*, 2020, pp. 4194–4201.

[18] J. G. Kassakian, M. F. Schlecht, and G. C. Verghese, *Principles of Power Electronics*. Addison-Wesley Publishing Company, 1991.

[19] P. Huynh, "An integrated generator-rectifier system for high-power ac-to-dc conversion," Ph.D. dissertation, University of Illinois at Urbana-Champaign, 2021.

[20] T. Bruckner, S. Bernet, and H. Guldner, "The active npc converter and its loss-balancing control," *IEEE Transactions on Industrial Electronics*, vol. 52, no. 3, pp. 855–868, June 2005.

[21] N. Celanovic and D. Boroyevich, "A comprehensive study of neutral-point voltage balancing problem in three-level neutral-point-clamped voltage source PWM inverters," *IEEE Transactions on power electronics*, vol. 15, no. 2, pp. 242–249, 2000.

[22] J. Birk and B. Andresen, "Parallel-connected converters for optimizing efficiency, reliability and grid harmonics in a wind turbine," in *2007 European Conference on Power Electronics and Applications*, Sep. 2007, pp. 1–7.

[23] B. Wu, Y. Li, and S. Wei, "Multipulse diode rectifiers for high-power multilevel inverter fed drives," in *9th IEEE International Power Electronics Congress, 2004. CIEP 2004*, Oct 2004, pp. 9–14.

[24] A. D. Gerlando, G. Foglia, M. F. Iacchetti, and R. Perini, "Analysis and test of diode rectifier solutions in grid-connected wind energy conversion systems employing modular permanent-magnet synchronous generators," *IEEE Transactions on Industrial Electronics*, vol. 59, no. 5, pp. 2135–2146, May 2012.

[25] N. Bianchi and M. Dai Prè, "Use of the star of slots in designing fractional-slot single-layer synchronous motors," *IEE Proceedings-Electric Power Applications*, vol. 153, no. 3, pp. 459–466, 2006.

[26] J. Faiz and I. Tabatabaei, "Extension of winding function theory for nonuniform air gap in electric machinery," *IEEE Transactions on Magnetics*, vol. 38, no. 6, pp. 3654–3657, 2002.

[27] N. L. Schmitz and D. W. Novotny, *Introductory Electromechanics*. University Microfilms, 1984.